Electronic Supplementary Information (ESI)

Chirality-tuned Magnetic Susceptibility of Chiral Mesostructured Cobalt Oxide Films

Liuliu He[a], Wenjun Zhu[a], Yang Gao[a], Quanzheng Deng[a] and Yingying Duan*[a]

Experimental Section

1. Chemicals

$Co(NO_3)_2 \cdot 6H_2O$, $NH_3 \cdot H_2O$, PVP(8000), L/D-Histidine, $KMnO_4$ and ethanol were purchased from Sinopharm Chemical Reagent Co., Ltd. The purity of all the reagents are ≥99%, which were used as received without further purification. The deionized (DI) water was obtained from a Milli-Q synthesis system.

2. Substrate activation

The quartz substrates (40×10×1 mm) were washed with a mixture of acetone and ethanol (V/V = 1:1) and deionized water in an ultrasonic bath for 30 min. For the surface activation, the substrates were placed in glass vials filled with 20 mL of 10 mM fresh $KMnO_4$ solution and 50 μL of *n*-butanol (as a reducing agent for the $KMnO_4$) at 85 ºC for 20 min. Permanganate-treated quartz wafers were then thoroughly rinsed in deionised water and sonicated for 10 min

3. Synthesis of CMCFs

In a typical synthesis, 0.12 g PVP, 2.0 mmol Histidine, 1.0 mmol $Co(NO_3)_2 \cdot 6H_2O$ were dissolved in 30 mL ultrapure water and stirred for 30 min. Subsequently, $NH_3 \cdot H_2O$ was introduced into the mixture, which was stirred for 10 minutes, and the pH was adjusted to a range of 10 to 11. Then the mixture and activated quartz wafer were transferred into 50 mL Teflon-line autoclaves to react under static conditions at 180 ºC for 20 h. After cooled down naturally to room temperature, the products were washed several times using ultrapure and then dried at 60 ºC overnight. Finally, the products were obtained by calcination at 550 ºC in air for 5 h with a heating rate of 1 ºC per minute.

4. Characterization

Wide XRD patterns were recorded on a Rigaku MiniFlex 600 powder diffractometer equipped with Cu Kα radiation, at the rate of 0.2 $^{o} \cdot min^{-1}$ over the range 10-80º. GIA-XRD patterns were recorded on a Rigaku SmartLab 9 kW powder diffractometer equipped with Cu Kα radiation, at the rate of 1 $^{o} \cdot min^{-1}$ over the range 10-80º. SEM images were obtained using JEOL JSM-7100 with accelerating voltage of 3 kV. The CD and MCD spectra were obtained on a JASCO J-1500 spectropolarimeter fitted with DRCD and MCD apparatus, and the data were collected with a scanning rate of 500 $nm \cdot min^{-1}$ ranging from 200 to 800 nm. The hysteresis curves of the samples were measured using a Superconducting Quantum Interference Device (SQUID) based magnetic measurement system (Quantum Design, USA) with magnetic fields in the range of -3-3 T at room temperatures. FTIR spectra were recorded using Bruker 2022-IS20. XPS data were collected using AXIS Ultra DLD.

Supplementary Figures and Tables

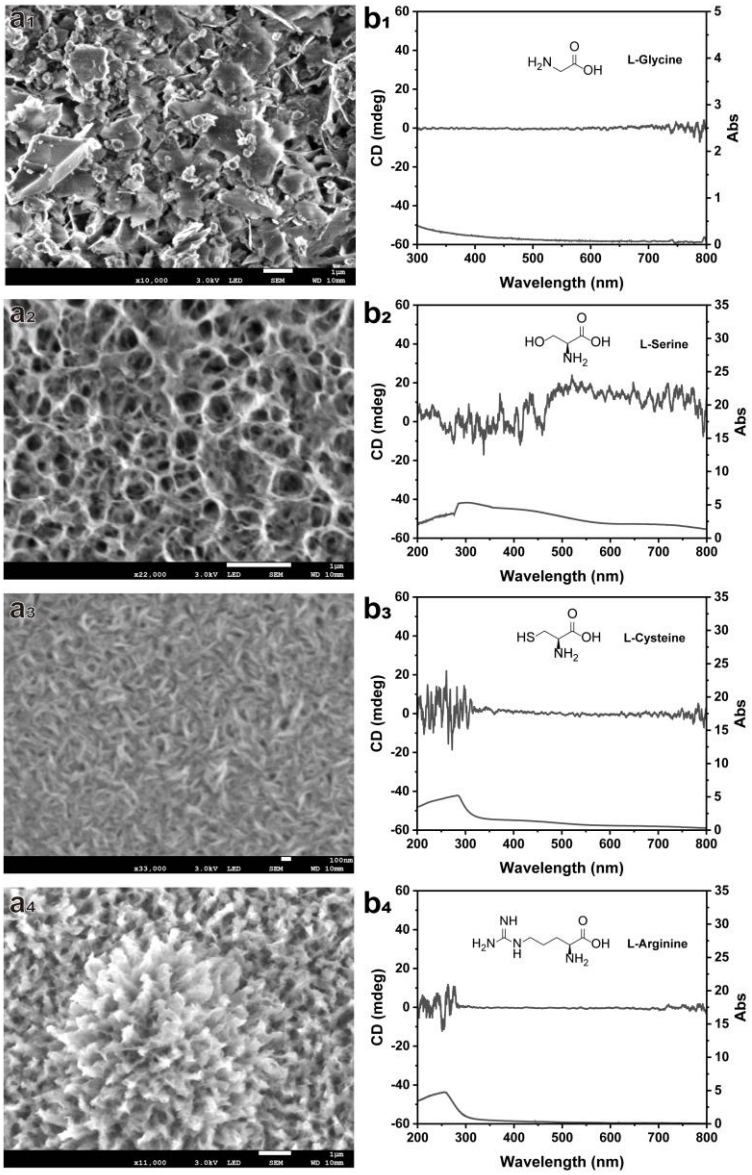

Figure S1. (a) SEM images and (b) transmission CD spectra of cobalt oxide thin films synthesized via induction by L-Glycine, L-Serine, L-Cysteine, and L-Arginine.

The cobalt oxide films synthesized under the induction of L-Glycine, L-Cysteine, and L-Arginine all exhibit no significant CD signal, whereas the film induced by L-Serine shows a weak peak in the range of 450–550 nm. From the perspective of surface morphology, amino acids with longer side chains at the α-carbon tend to form films more readily on the substrate. Moreover, when the carboxyl and amino groups are attached to adjacent carbon atoms, the resulting nanosheets display tighter packing and more pronounced misalignment structures. These structural features further promote the formation of chirality.

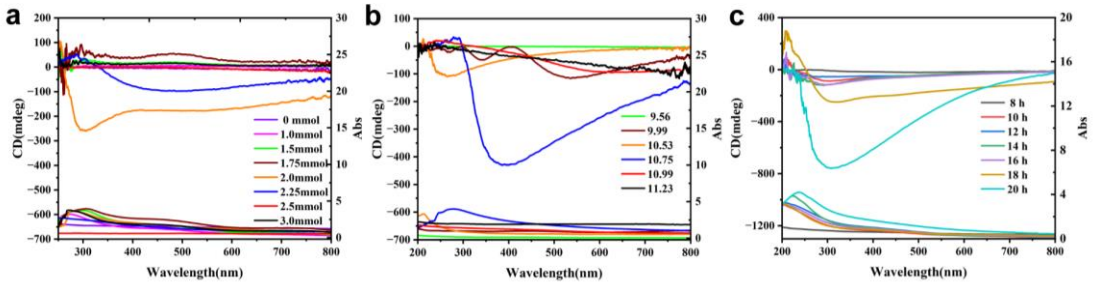

Figure S2. (a) CD spectra of L-CMCFs synthesized by adjusting different molar amounts of L-histidine; (b) Transmission CD spectra of L-CMCFs synthesized under different pH conditions regulated by aqueous ammonia; (c) Transmission CD spectra of L-CMCFs synthesized under different pH conditions regulated by aqueous ammonia.

As shown in Fig. S2a, the optimal CD signal is achieved when the amount of L-histidine added is 2 mmol. This indicates that chiral induction is weak at low chiral molecule concentrations; it increases significantly with rising concentration; however, at high concentrations, the efficiency of chiral induction declines due to multiple factors such as disruption of the coordination equilibrium between metal ions and chiral molecules and intermolecular competition.

The characterization results of CD are shown in Fig. S2b. At approximately pH 10.70, the CD signal peak reaches its maximum intensity, approaching 450, indicating that the ammonia-induced synthesis of chiral cobalt oxide is optimal under this pH condition. As the solution pH increases, the CD signal peak of the sample undergoes a redshift, primarily due to the increase in size of the chiral nanosheets (Fig. S3). As shown in Fig. S2c, increasing the reaction time to 20 h resulted in the strongest chiroptical activity, indicating a relatively strong chiral dislocation assembly at this stage.

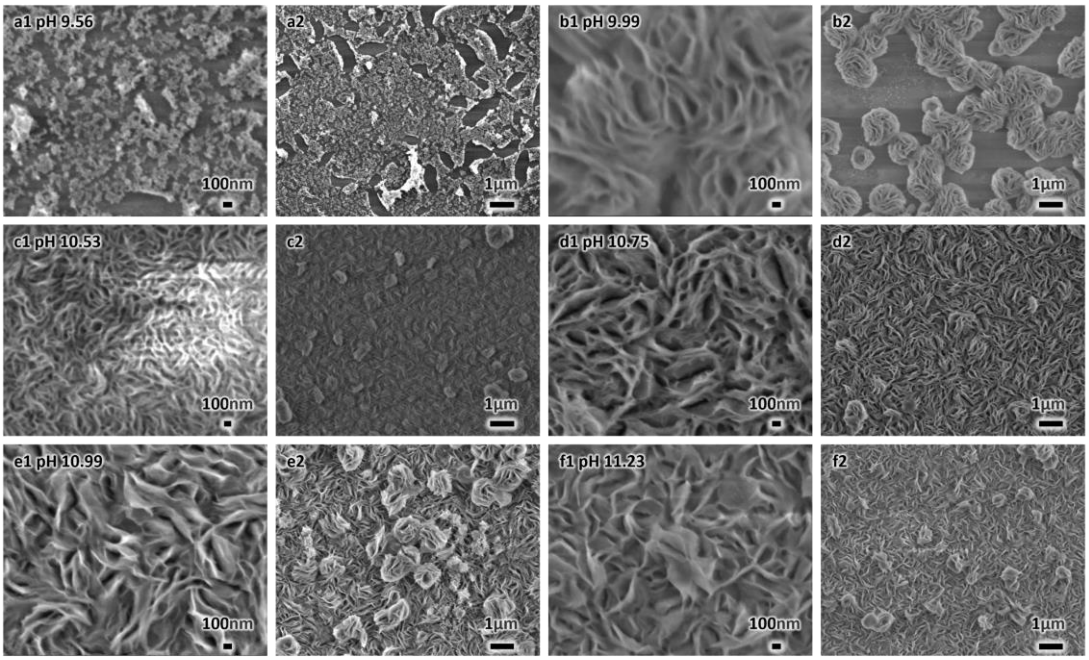

Figure S3. SEM images of L-CMCFs synthesized under different pH conditions regulated by aqueous ammonia at various magnifications.

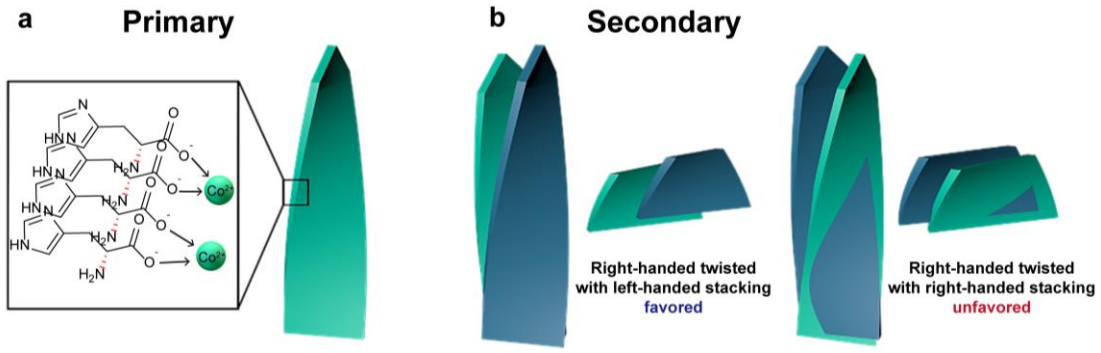

Figure S4. Illustration of chirality transfer from chiral organic molecule to D-CMCFs.

As shown in Fig. S9a, the chiral primary structure with right-handed distorted crystal lattice would be induced by the D-His, in which the carboxyl and amino groups chelated well with the Co^{2+}. As the concentration of OH^- increases in the solution, OH^- replaces His in coordinating with cobalt ions, enhancing the rigidity of the lamellar structure and transforming it into a hydroxide phase. This hydroxide subsequently grows into nanosheets on the hydroxylated quartz substrate. Throughout this process, the primary chirality of the nanosheets is obtained by replicating the molecular chirality of His, which induces a chiral growth orientation. The secondary chiral structure tends to exhibit a handedness opposite to that of the primary chirality through chiral dislocation, ultimately forming a cobalt oxide film with a secondary chiral architecture.

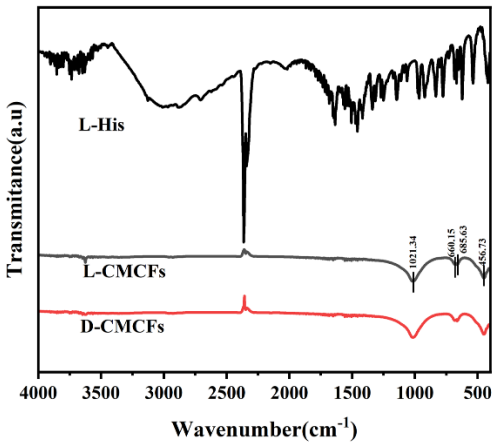

Figure S5. FTIR spectra of L-Histidine and 10D- and 10L-CMCFs.

The FTIR spectrum is divided into two primary regions: the material fingerprint region (400-1000 cm^{-1}) and the functional group region (1000-4000 cm^{-1}). A weak absorption band observed at around 2300 cm^{-1} is attributed to the C=O stretching vibration resulting from atmospheric CO_2. Additional bands near 1000 cm^{-1} and 456.73 cm^{-1} correspond to Co-O stretching vibrations, while those at 660.15 cm^{-1} and 685.63 cm^{-1} are characteristic of the Co_3O_4 spinel structure. Compared with the FTIR spectrum of histidine, no C-H or O-H vibrational bands are detected aside from the atmospheric CO_2 contribution, confirming the complete removal of organic species.

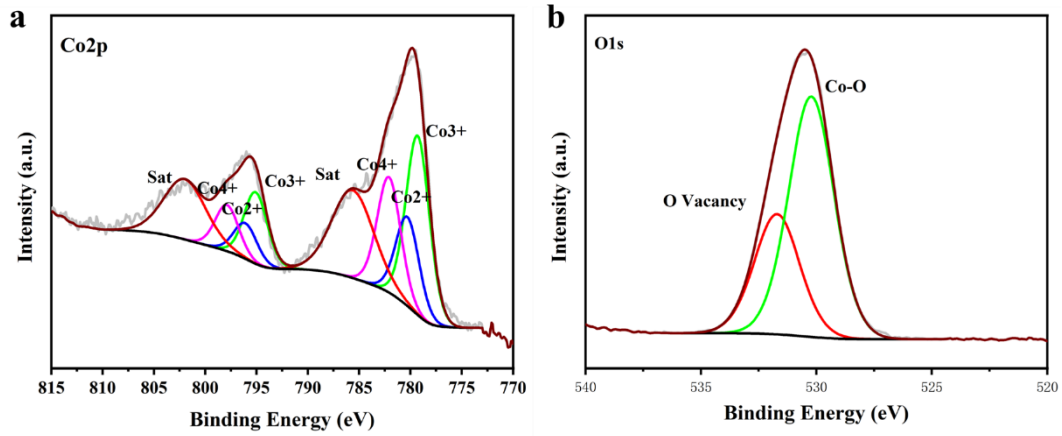

Figure S6. XPS spectra of Co 2p (a) and O 1s (b).

The XPS spectrum of Co 2p is presented in Fig. S5a. Due to spin-orbit coupling, the spectrum splits into two main regions: Co $2p_{3/2}$ (780-790 eV) and Co $2p_{1/2}$ (795-805 eV). The peaks observed at 780.3 eV and 796.2 eV are assigned to Co^{2+}, those at 779.3 eV and 795.2 eV correspond to Co^{3+}, and the signals at 782.1 eV and 797.7 eV are attributed to Co^{4+}. In addition, satellite peaks are identified at 785.6 eV and 802.1 eV.

As shown in Fig. S5b, the O 1s spectrum exhibits binding energies in the range of 520-540 eV. The peak at 530.2 eV is primarily associated with lattice oxygen in Co-O bonds, while the peak at 531.7 eV corresponds to oxygen vacancies. These results confirm the successful synthesis of chiral cobalt oxide films with mixed valence states.

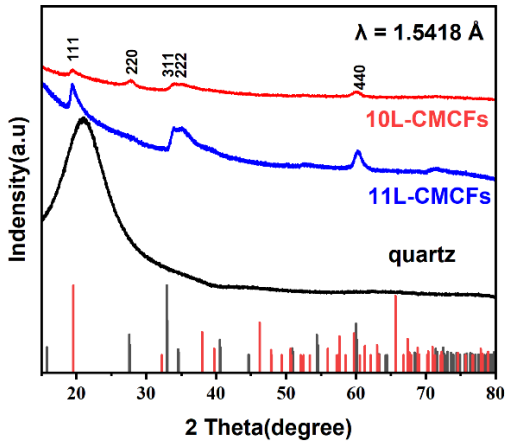

Figure S7. GIA-XRD patterns of 10L- and 11L-CMCFs.

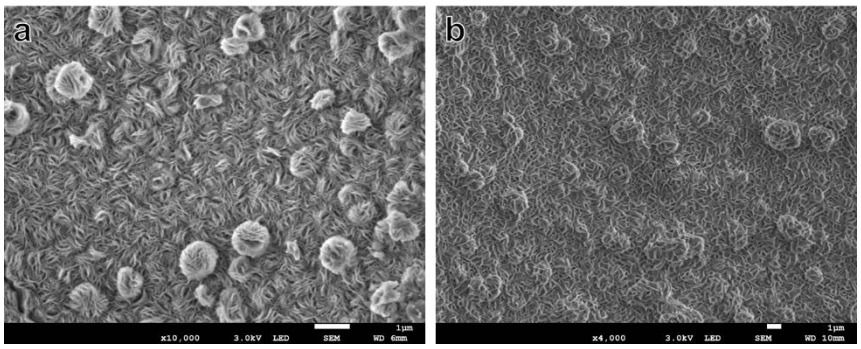

Figure S8. SEM images of 10D-(a) and 11D-(b) CMCFs at low magnification.

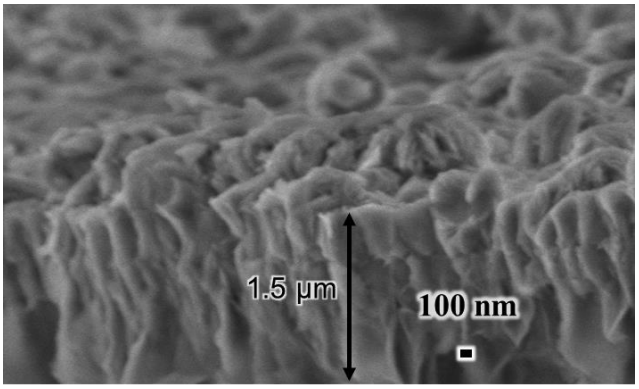

Figure S9. Side view SEM images of 10D-CMCF.

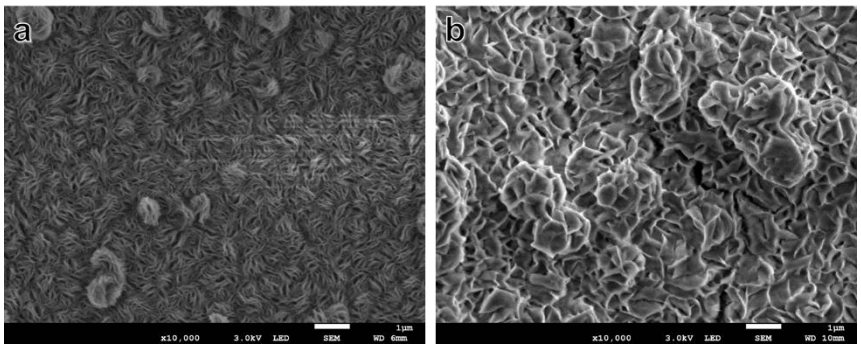

Figure S10. SEM images of 10L-(a) and 11L-(b) CMCFs.

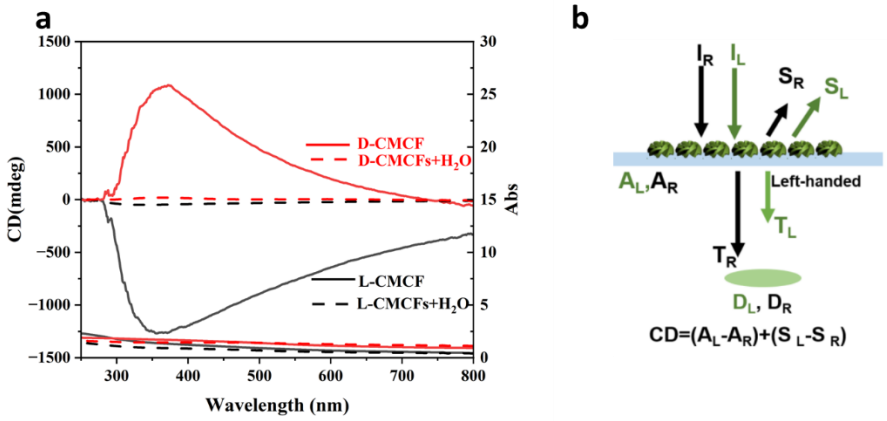

Figure S11. Transmitted UV-Vis and CD Spectra of antipodal 10-CMCFs (solid lines) and those infiltrated with water (dash lines).

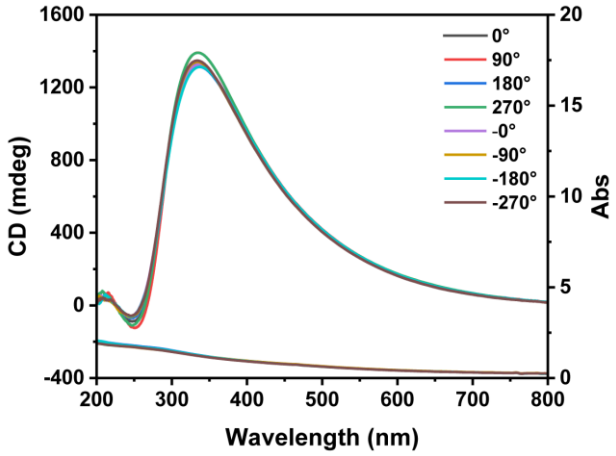

Figure S12. Transmitted CD spectra of 10D-CMCFs measured on both sides of the film and at four different angles.

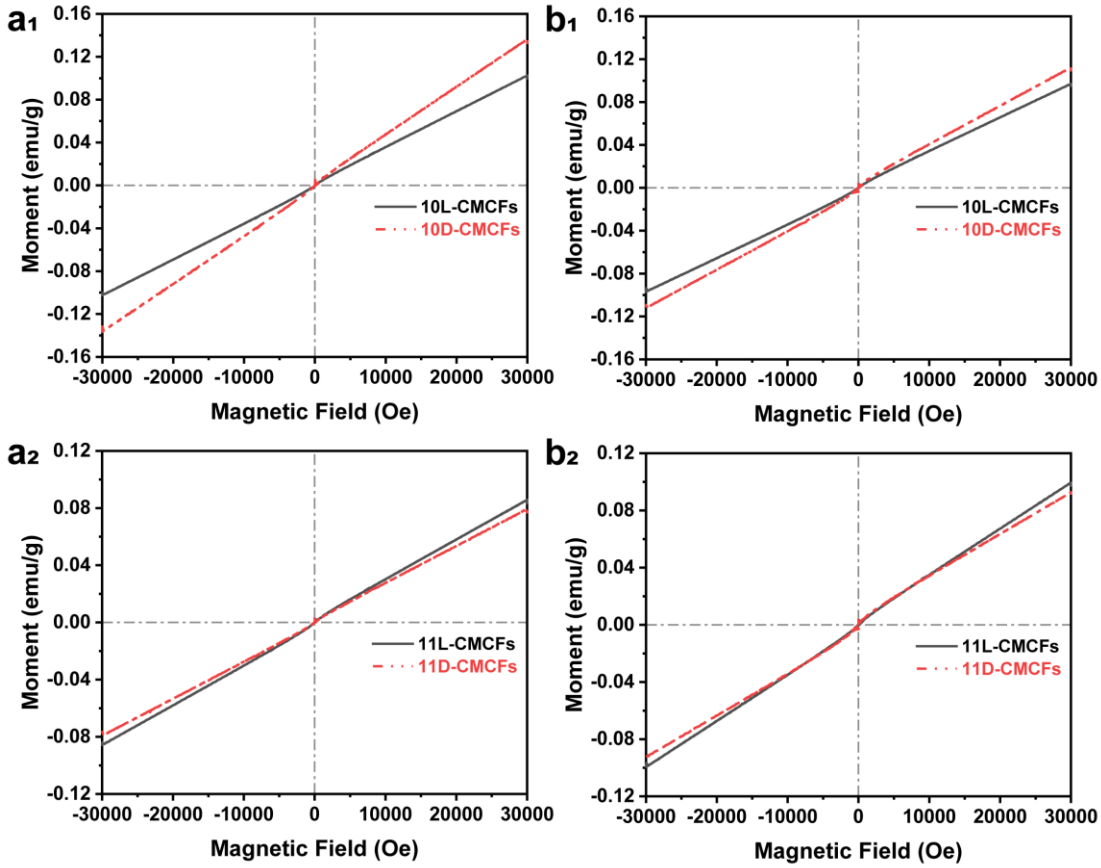

Figure S13. M-H curves of another two pairs of antipodal (a) 10-CMCFs and (b) 11-CMCFs.

The magnetic susceptibility (χ) of 10D-CMCF (4.595×10^{-6} emu·g^{-1}·Oe^{-1}) was found to be higher than that of 10L-CMCF (3.455×10^{-6} emu·g^{-1}·Oe^{-1}) with increasing magnetic field (Figure S13a$_1$). In contrast, for the 11-CMCFs with opposite chiral structures, the magnetic susceptibility of 11L-CMCF (2.898×10^{-6} emu·g^{-1}·Oe^{-1}) was observed to be higher than that of 11D-CMCF (2.669×10^{-6} emu·g^{-1}·Oe^{-1}) with increasing magnetic field strength (Figure S13a$_2$). Consistently, in another batch of samples (Figure S13b), 10D-CMCF (3.815×10^{-6} emu·g^{-1}·Oe^{-1}) exhibited higher magnetic susceptibility than 10L-CMCF (3.279×10^{-6} emu·g^{-1}·Oe^{-1}), and the magnetic susceptibility of 11L-CMCF (3.359×10^{-6} emu·g^{-1}·Oe^{-1}) was higher than that of 11D-CMCF (3.169×10^{-6} emu·g^{-1}·Oe^{-1}). These comparative results across different batches are consistent with the findings in the main manuscript, thereby validating the reproducibility of the observed magnetic susceptibility trends in CMCFs.

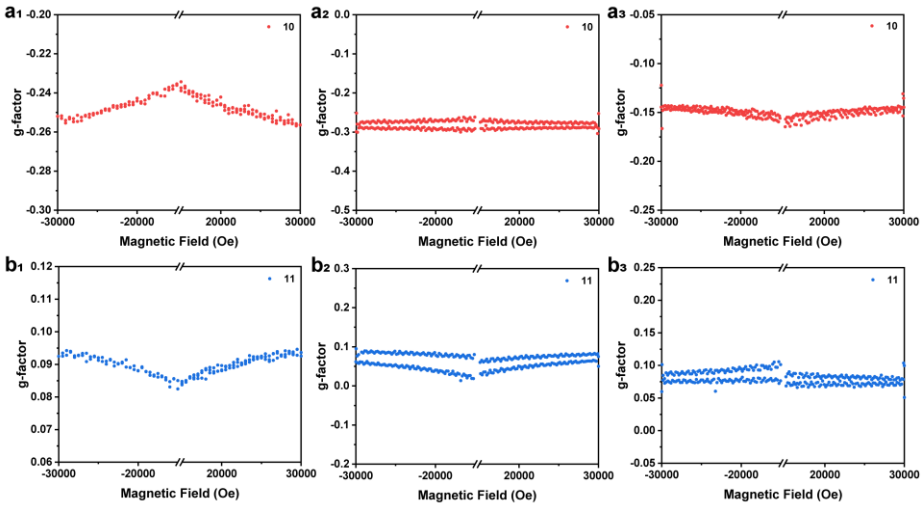

Figure S14. G-factors of different batches of (a) 10-CMCFs and (b) 11-CMCFs.

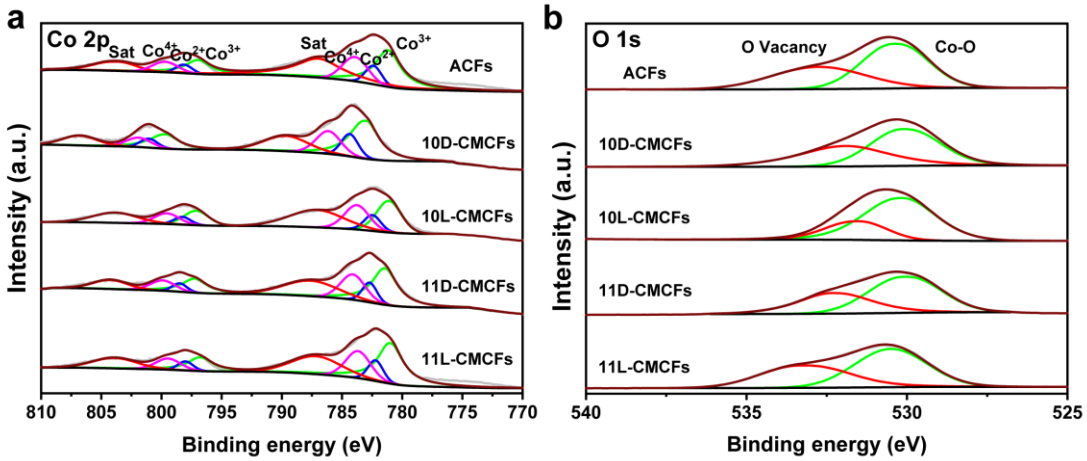

Figure S15. XPS spectra of Co 2p (a) and O 1s (b).

We conducted X-ray photoelectron spectroscopy (XPS) analysis on the 10-CMCFs, 11-CMCFs, and ACFs samples. This was done to verify that the chemical valence states of the cobalt oxides are consistent across both the enantiomeric and achiral configurations. The Co 2p XPS spectrum is presented in Fig. S15a. Due to spin-orbit coupling, the spectrum splits into two distinct regions: Co $2p_{3/2}$ and Co $2p_{1/2}$. The observed peaks correspond to Co^{2+}, Co^{3+}, and Co^{4+}, accompanied by satellite signals. As shown in Fig. S15b, the O 1s spectrum reveals features associated with lattice oxygen in Co–O bonds and oxygen vacancies. These XPS results, which are entirely consistent with the supplementary data in Figure S6, collectively confirm that both the enantiomeric and achiral cobalt oxides exhibit identical mixed-valence states. This finding effectively rules out differences in oxidation states as a contributing factor to the observed CISS effect.

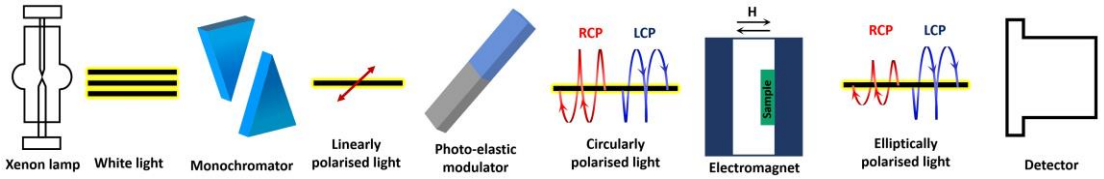

Figure S16. Magnetic circular dichroism (MCD) experimental set-up.

A light from a broad-band emitting source is passed through a monochromator and polarizer to generate a monochromatic linearly polarized beam. A portion of this beam is passed through a photo-elastic modulator creating L- and R-CP light. A sample is placed in an electromagnet with the lines of the magnetic field oriented parallel to the light propagation direction. Upon passing through the sample L-CP and R-CP light are absorbed to a different degree. Different intensities of L- and R-CP light are combined to form an elliptically polarized beam. MCD is the difference of absorption toward L- (A_L) and R-CP light (A_R) under the magnetic field.

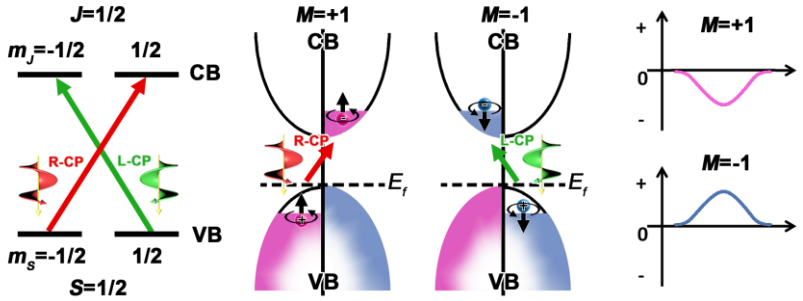

Figure S17. The simplified diagram of magnetic circular dichroism (MCD).

As shown in schematic of the optical orientation of excitons by CP light in bulk semiconductors, In the ground state, the VB is completely filled with equal populations in spin-up and spin-down states. Following R-CP light excitation with photon energy near the bandgap, electrons make transitions from the VB to the CB, and leave spin-up holes in the VB. One +1/2 electron and one spin-up hole are bound together to form a spin-polarized exciton with angular momentum projection M=+1. Similarly, L-CP light excites and exciton state with M=-1. The exciton recombination is much slower than spin relaxation, and thus not relevant in the spin dynamics measurement. Hence the MCD spectroscopy allows optical orientation and detection of spin-polarized excitons.

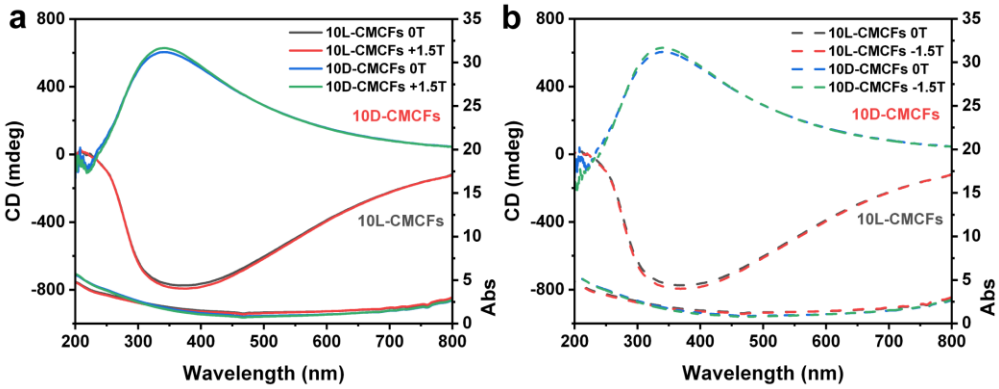

Figure S18. CD spectra of 10D-CMCFs and 10L-CMCFs under positive (a) and negative (b) applied magnetic fields.

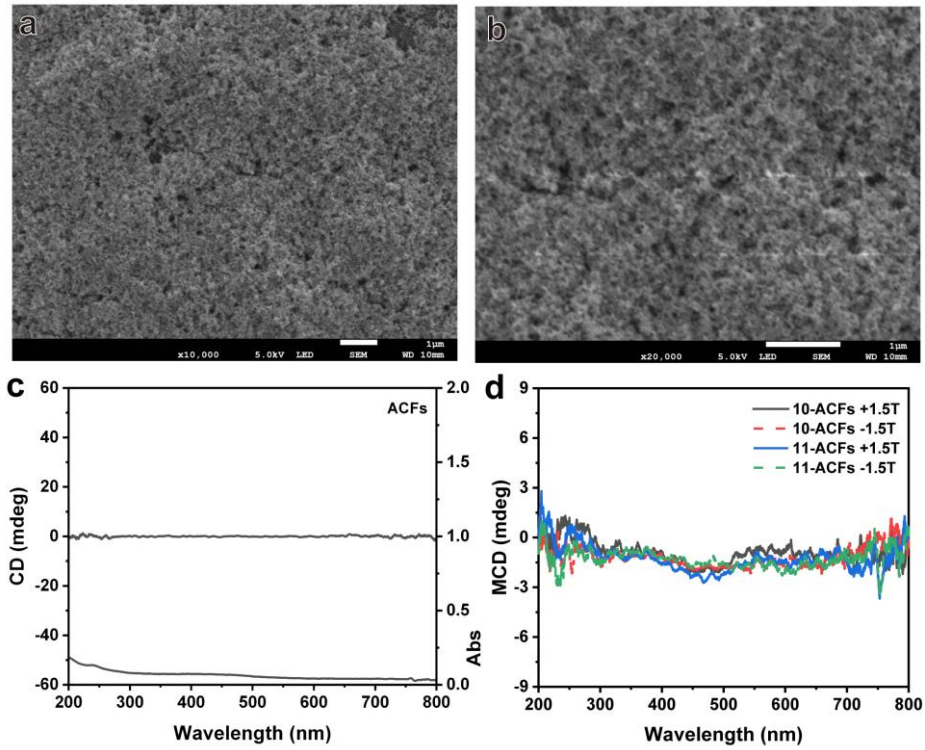

Figure S19. (a, b) SEM images of various magnification of ACFs. (c) UV-Vis and CD spectra of ACFs. (d) MCD spectra of ACFs. The achiral cobalt oxide films were synthesized in the same routes as the CMCFs without adding the histidine.

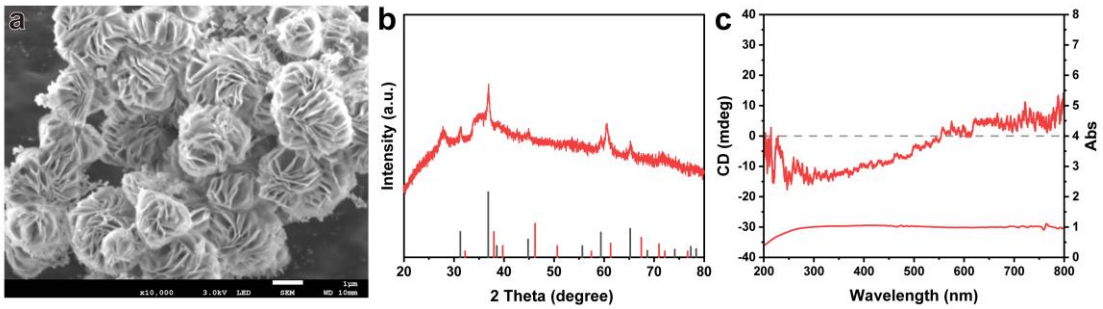

Figure S20. (a) SEM image, (b) XRD pattern and (c) DRCD and DRUV-Vis spectra of 10L-CMCPs.

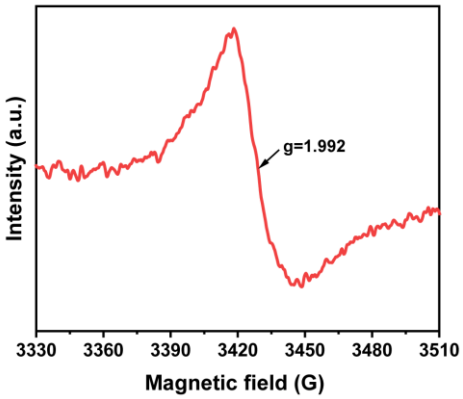

Figure S21. EPR spectra of 10L-CMCPs.

To check whether the materials themselves possess paramagnetic character, we measured powder samples—chiral mesostructured cobalt oxide powders (CMCPs)—obtained from the same synthesis. As shown in Figure S18, 10L-CMCPs exhibit the same nanosheet morphology, XRD pattern and CD signal as 10L-CMCFs, confirming structural identity. Their EPR spectrum (Figure S19) displays a clear signal with a g-value of 1.992, characteristic of oxygen vacancies (OVs) in cobalt oxide. OVs are known to introduce spin-polarized electrons. Since the powder and thin films are structurally identical, this result provides indirect but strong evidence for the presence of similar spin-polarized centers in the chiral thin films.